

Breakdown of potential vorticity–based equivalent latitude as a vortex-centered coordinate in the polar winter mesosphere

V. Lynn Harvey,¹ Cora E. Randall,^{1,2} and Matthew H. Hitchman³

Received 17 June 2009; revised 23 August 2009; accepted 3 September 2009; published 24 November 2009.

[1] Potential vorticity (PV) and stream function (ψ) are useful vortex-centered coordinates for studying the winter stratosphere, since both exhibit monotonic relationships with tracer constituents. At each isentropic level in the stratosphere and mesosphere, ψ varies monotonically normal to the jet axis and to tracer contours, and can thus be considered vortex-centered. In the stratosphere, PV is anticorrelated with ψ and is also vortex-centered. We show that, contrary to this, above ~ 3000 K (~ 60 km) the PV- ψ anticorrelation breaks down up to 80% of the time. Over five years of Goddard Earth Observing System analyses are used to depict the seasonal and spatial variation of the relationship between PV and ψ . The deviation of PV from a vortex-centered coordinate is estimated by calculating differences between the mean latitude of the highest PV band and the most polar mean latitude for any PV band in the hemisphere. If PV is anticorrelated with ψ , and thus vortex centered, these differences should be small. In both winter hemispheres, latitude differences are less than 5° below 55 km but exceed 15° above 60 km (~ 0.5 hPa, ~ 3000 K). In the mesosphere, regions of small PV are usually found in the vortex core and the largest PV values are located along the subtropical jet. The relationship between PV and ψ in the polar lower mesosphere is interpreted in the context of the gravity wave driven warm anomaly, the associated wave breaking regime, and local static stability anomalies which affect PV much more than ψ .

Citation: Harvey, V. L., C. E. Randall, and M. H. Hitchman (2009), Breakdown of potential vorticity–based equivalent latitude as a vortex-centered coordinate in the polar winter mesosphere, *J. Geophys. Res.*, 114, D22105, doi:10.1029/2009JD012681.

1. Introduction

[2] The winter stratospheric polar vortex is characterized by a strong westerly circumpolar jet that forms as a result of the absence of shortwave heating by ozone in the polar night, the polar night jet (PNJ) [e.g., Schoeberl *et al.*, 1992]. Large descent rates in the vortex [e.g., Fisher *et al.*, 1993; Manney *et al.*, 1994; Rosenfield *et al.*, 1994] and homogenization by Rossby wave breaking (RWB) [e.g., McIntyre and Palmer, 1983; Baldwin and Holton, 1988; Rhines and Young, 1982] create a polar vortex air mass that is distinctly different from air outside the vortex. The polar air mass is the site of polar stratospheric cloud-induced ozone depletion in the lower stratosphere [e.g., Solomon, 1999] and energetic particle-induced production of odd nitrogen in the upper stratosphere and mesosphere [e.g., Randall *et al.*, 2006, 2007, 2009]. Poleward RWB occurs contemporaneously with equatorward RWB on the PNJ [Hitchman and

Huesmann, 2007], creating distinctive polar and midlatitude air masses. Immediately equatorward of the jet maximum differential advection shears eddies into filaments, leading to pronounced gradients in potential vorticity (PV) and trace constituents, characterized by densely interlayered ribbons of air from the two air masses, with attendant mixing [e.g., Proffitt *et al.*, 1992; Lahoz *et al.*, 1994]. In the stratosphere, the relationship between PV and trace constituents is extremely useful for diagnostic interpretation and assimilation of satellite trace constituents into global chemical transport models [e.g., Manney *et al.*, 1999, 2007, 2009a, 2009b; Stajner *et al.*, 2004; Randall *et al.*, 2005].

[3] The polar mesospheric mean meridional circulation is characterized by rising air over the summer pole and sinking air over the winter pole. Haurwitz [1961] and Leovy [1964] showed that it is driven by the absorption of gravity waves atop the winter westerly and summer easterly stratospheric jets. The resulting gravity wave driven warm anomaly descends during winter by nonlinear wave–mean flow interaction, creating a separated polar winter stratopause [Hitchman *et al.*, 1989; Danielsen, 1990; Garcia and Boville, 1994]. It is known that the PNJ is located at lower latitudes in the mesosphere than in the stratosphere due to this polar warm anomaly [Dunkerton and Delisi, 1985]. This structure leads to an unusually vigorous wave breaking regime in the polar lower mesosphere, which, as will be shown, involves shallow temperature anomalies.

¹Laboratory for Atmospheric and Space Physics, University of Colorado at Boulder, Boulder, Colorado, USA.

²Department of Atmospheric and Oceanic Sciences, University of Colorado at Boulder, Boulder, Colorado, USA.

³Department of Atmospheric and Oceanic Sciences, University of Wisconsin-Madison, Madison, Wisconsin, USA.

[4] Widely used to understand flow and static stability structure, Ertel's PV (given as P in equations) is the product of absolute vorticity and static stability:

$$P = (f + \zeta)/\sigma, \quad (1)$$

where $f = 2\Omega \sin \phi$ is the local vertical component of planetary vorticity, $\zeta = \partial v/\partial x - \partial u/\partial y$ is relative vorticity, σ is isentropic density ($\text{kg m}^{-2} \text{K}^{-1}$), and $1/\sigma = -g \partial \theta/\partial p = (1/\rho) \partial \theta/\partial z$ is static stability [Ertel, 1942]. Variables follow the notation of Andrews *et al.* [1987]. The distribution of PV provides insight into inertial and convective instabilities, Rossby wave dynamics, the development of weather systems, and barotropic and baroclinic instabilities [Hoskins *et al.*, 1985]. Due to the Coriolis parameter, PV normally increases monotonically from large negative values at the South Pole to large positive values at the North Pole. Meridional reversals in the PV gradient are indicative of RWB and irreversible mixing which violates PV conservation. Due to the upward decrease of density, PV generally increases with increasing altitude.

[5] A crucial aspect of PV is that it includes a vertical derivative of temperature, while stream function ψ (and hence the relative vorticity component of PV) is a vertical integral of temperature. These mathematical definitions allow for the possibility that vertically local temperature anomalies can influence PV much more than ψ , and provide the core of our explanation for the observed relationship between PV and ψ in the polar lower mesosphere.

[6] Since the meridional profile of the zonal wind across a westerly jet maximum is negatively curved ($\partial^2 u/\partial y^2 < 0$), the PV gradient is enhanced at the jet maximum. Thus, the PV gradient maximum is useful for identifying the jet axis [e.g., Rummukainen *et al.*, 1994; Nash *et al.*, 1996] at the edge of the polar vortices. In the stratosphere, the PV contour determined to represent the vortex edge agrees well with vortex edge calculations using other techniques [e.g., Waugh, 1997; Harvey *et al.*, 2002]. Butchart and Remsberg [1986] employed the prevalent monotonic PV increase from the tropics to the center of the boreal stratospheric polar vortex in a novel fashion, using PV to compute equivalent latitudes for categorizing constituent distributions. An equivalent latitude circle for a given value of PV encloses the same area as the total area of air with PV exceeding that value in the hemisphere. Geographically separated but similar air masses, with characteristic values of PV and constituent concentrations, are combined in equivalent latitude bins. This procedure for combining like air masses is more appropriate than averaging around latitude circles when zonal asymmetries exist. Many authors have used PV-based equivalent latitude as a useful vortex-centered meridional coordinate in the stratosphere [e.g., Norton, 1994; Lary *et al.*, 1995; Randall *et al.*, 2005; Ren and Cai, 2006; Stan and Randall, 2007; Manney *et al.*, 1999, 2007, 2008b].

[7] Allen and Nakamura [2003] showed that near the stratopause, PV equivalent latitude sometimes has a local minimum in the vortex that is not observed in tracer equivalent latitude (TrEL). Tracer contours are observed as concentric loops that encircle the polar vortex [Nakamura, 1995; Nakamura and Ma, 1997]. Since tracer concentrations generally vary monotonically poleward of the jet axis, the TrEL approach yields a vortex-centered coordinate at

both low and high altitudes. Upper stratospheric and lower mesospheric observations suggest that the horizontal distribution of PV in the mesosphere can be quite complex [e.g., Manney *et al.*, 2008a, 2009b, and references therein]. Filipiak *et al.* [2005] showed evidence that carbon monoxide (CO) from the microwave limb sounder (MLS) and PV are not well correlated in the mesosphere, although Pumphrey *et al.* [2007] cautioned that MLS CO may be somewhat noisy in the mesosphere. Lahoz *et al.* [2009] showed differences between horizontal distributions of PV derived using European Centre for Medium-range Weather Forecasting (ECMWF) analyses and methane observed by the Michelson Interferometer for Passive Atmospheric Sounding (MIPAS) instrument.

[8] This work explores the relationship between ψ and PV from 500 to 4600 K and its evolution during winter in both hemispheres. The Goddard Earth Observing System (GEOS) analyses from which ψ and PV are computed are described in section 2, as well as a description of MLS temperature and CO. The seasonal, latitudinal, and altitudinal dependence of the utility of PV and ψ for interpreting constituent distributions is shown in Section 3, including an estimate of the fraction of time for which PV or ψ is not useful as a vortex-centered coordinate. These results are interpreted in terms of physical processes in Section 4, which focuses on static stability structures and effects on PV and ψ . Conclusions are given in Section 5.

2. Meteorological Analyses and Satellite Data

2.1. GEOS-5 Assimilated Analyses

[9] This work uses analyses from the NASA Global Modeling and Assimilation Office's (GMAO) GEOS versions 5.1 and 5.2 (after August 2008) [Rienecker *et al.*, 2008, and references therein]. GEOS-5 analyses are produced using the Grid point Statistical Analysis method of Wu *et al.* [2002], a three-dimensional variational assimilation system, with a 6 hour analysis window. The atmospheric model makes use of a finite-volume dynamical core [Lin, 2004]. The model assimilates operational meteorological products, column ozone from the Solar Backscattered Ultraviolet (SBUV) and SBUV/2 instruments [Stajner *et al.*, 2004], and microwave and infrared radiances from the Special Sensor Microwave Imager and Atmospheric Infrared Sounder instruments, as described by Stajner *et al.* [2007]. An incremental analysis update approach is used to reduce shocking the model following the insertion of observations [Bloom *et al.*, 1996]. The model incorporates two gravity wave drag parameterizations, an orographic gravity wave drag formulation based on McFarlane [1987], and a formulation for nonorographic waves based on Garcia and Boville [1994]. These are tuned to yield realistic stratospheric and mesospheric temperatures and wind fields in the free-running model (S. Pawson, personal communication, 2008). In this work, GEOS-5 analyses of pressure, temperature, geopotential height, horizontal winds, and PV are used. Analyses are provided every 6 hours at 72 vertical levels from 1 km to 72 km, on a 0.5° latitude by $2/3^\circ$ longitude grid.

[10] Daily averaged products are linearly interpolated to a 2.5° latitude by 3.75° longitude grid and to potential temperature levels ranging from 500 K (~ 20 km) to 4600 K

(~ 75 km). The vertical resolution of the isentropic surfaces is 100 K between 500 K and 1000 K, and 200 K between 1000 K and 4600 K. This vertical resolution corresponds to altitude increments of ~ 3 km near 25 km altitude, decreasing to ~ 1.5 km near 75 km altitude. We compared the coarse analyses to the original resolution analyses, and the large-scale wind and PV fields are similar; both show a jet maximum in the mesosphere that is at lower latitude than in the stratosphere and weak PV gradients at higher latitudes. In our analysis we estimate a rotational stream function ψ , which is obtained by separating the velocity field into divergent and rotational components, and solving the inverse Laplacian: $\psi = (\partial^2/\partial x^2 + \partial^2/\partial y^2)^{-1} \zeta$. Results based on ψ are very similar to those based on the Montgomery stream function, $M = C_p T + g Z$, where C_p is the specific heat at constant pressure, T is in Kelvins, g is gravitational acceleration, and Z is geopotential height in m. Values of ψ are shown here in units of s^{-1} . For use in calculating wind and vorticity, ψ values should be multiplied by a^2 , where $a = 6.367 \times 10^6$ m, scaling for the inverse Laplacian.

[11] It is important to understand the validity of the GEOS-5 analyses. *Manney et al.* [2008a] compared GEOS-5 temperature and zonal winds to satellite observations during January and February 2006. In late January 2006 there was a major stratospheric warming event followed by a strengthening of the upper stratospheric vortex in February and reformation of the polar stratopause at very high altitude (~ 80 km). The stratopause in GEOS-5 reformed near 60 km and was 10–20 K warmer than MLS. Above 50 km, GEOS-5 zonal mean wind speeds (both easterlies and westerlies) were stronger than those derived from the Sounding of the Atmosphere using Broadband Emission Radiometry (SABER) instrument as well as from MLS temperatures [*Manney et al.*, 2008a]. Large differences between GEOS-5 and MLS stratopause altitude and temperature were also observed in the weeks following the warming event in late January 2009 [*Manney et al.*, 2009a]. These biases in the upper stratosphere and lower mesosphere are likely due to a lack of observations assimilated above the stratopause, deficiencies in the parameterization of gravity waves, and model tops that are too low. The reader is referred to *Manney et al.* [2008a, 2008b, 2009a, 2009b] for further comparisons between GEOS-5 and satellite data and for detailed analysis of the dynamical and trace gas evolution before, during, and after the 2006 and 2009 warming events.

[12] Comparisons between GEOS-5, MLS, and SABER temperatures are in better agreement when conditions are less disturbed (not shown). The large-scale structure of the elevated polar winter stratopause is captured in GEOS-5, albeit it is usually warmer than indicated by MLS. Likewise, during stratospheric warming events, the descent of the stratopause in GEOS-5 is in general agreement with MLS observations. With the exception of several weeks following stratospheric warming events in the Arctic in 2006 and 2009, the large-scale structure and morphology of the stratopause in GEOS-5 is in good agreement with MLS. Five-year latitude-time series show that the stratopause in GEOS-5 is ~ 10 K warmer and ~ 5 km higher than MLS inside the winter polar vortices in both hemispheres; the opposite is found outside the vortex in midlatitudes and during the summer (J. France et al., Comparison of GEOS-5,

SABER, and MLS stratopause height and temperatures, manuscript in preparation, 2009). The large-scale structure of the temperature field in GEOS-5 is in qualitative agreement with observations such that static stability distributions are of sufficient quality to support our conclusions. The present work relies on broadly consistent features between the GEOS-5 analyses and satellite observations, namely a lower-latitude mesospheric jet surrounding a warm anomaly at the pole. It will be argued that the change in relationship between PV and ψ is related to the vertically local temperature anomalies in the lower mesospheric surf zone [e.g., *Oberheide et al.*, 2006; *Sassi et al.*, 2002], rather than being a flaw in the temperature and wind analyses.

2.2. MLS Temperature and Carbon Monoxide

[13] This work uses MLS Version 2.2 temperature data to compute static stability for comparison with GEOS-5. MLS CO data are compared to GEOS-5 horizontal winds and ψ to support the assumption that, in the upper stratosphere and lower mesosphere, ψ remains a vortex-centered field. The MLS instrument is on NASA's Earth Observing System (EOS) Aura satellite that was launched on 15 July 2004 [*Waters et al.*, 2006] into a Sun-synchronous polar orbit. MLS measures thermal microwave emissions from the Earth's limb and provides measurements between 82° S to 82° N each day. Nearly 3500 vertical profiles are measured daily at 120 tangent altitudes. In the stratosphere and lower mesosphere, the profiles are spaced about 165 km apart along the orbit track. Temperature is determined from emissions of oxygen at 118 GHz below 1.41 hPa and at 118 GHz and 190 GHz from 1 hPa to 0.001 hPa. The vertical resolution is ~ 8 km at 1 hPa and ~ 9 km at 0.1 hPa. Systematic and random errors are 0.6 K in the lower stratosphere and 2.5 K in the mesosphere [*Schwartz et al.*, 2008]. *Schwartz et al.* [2008] used SABER, the Halogen Occultation Experiment (HALOE), the Atmospheric Chemistry Experiment (ACE), and radiosondes to show that MLS temperatures have a warm bias of 1–3 K in the stratosphere and a 0–7 K cold bias in the mesosphere. MLS temperature data are of sufficient quality for use in scientific studies from 316 hPa to 0.001 hPa (~ 90 km).

[14] MLS determines CO from emission at 240 GHz. The vertical resolution is 3–4 km below 60 km and 7–8 km above 60 km. In the mesosphere, CO mixing ratios have a 25% high bias compared to data from the Atmospheric Chemistry Experiment Fourier Transform Spectrometer [*Pumphrey et al.*, 2007; *Manney et al.*, 2007]. In the winter vortex, the descent of CO-rich air from the mesosphere to the stratosphere results in mixing ratios that are much larger than estimates of precision [*Pumphrey et al.*, 2007]. MLS CO data are of sufficient quality for use in scientific studies from 215 hPa to 0.0046 hPa (~ 85 km). For this work, the temperature and CO data have been filtered using the status, quality, threshold, and convergence values provided by the MLS science team [*Livesey et al.*, 2007].

3. Results

[15] Horizontal distributions of ψ and PV are shown in Figure 1 to illustrate the geographic location of ψ minima and PV maxima relative to the location of the polar night jet. Northern Hemisphere (NH) polar projections are shown

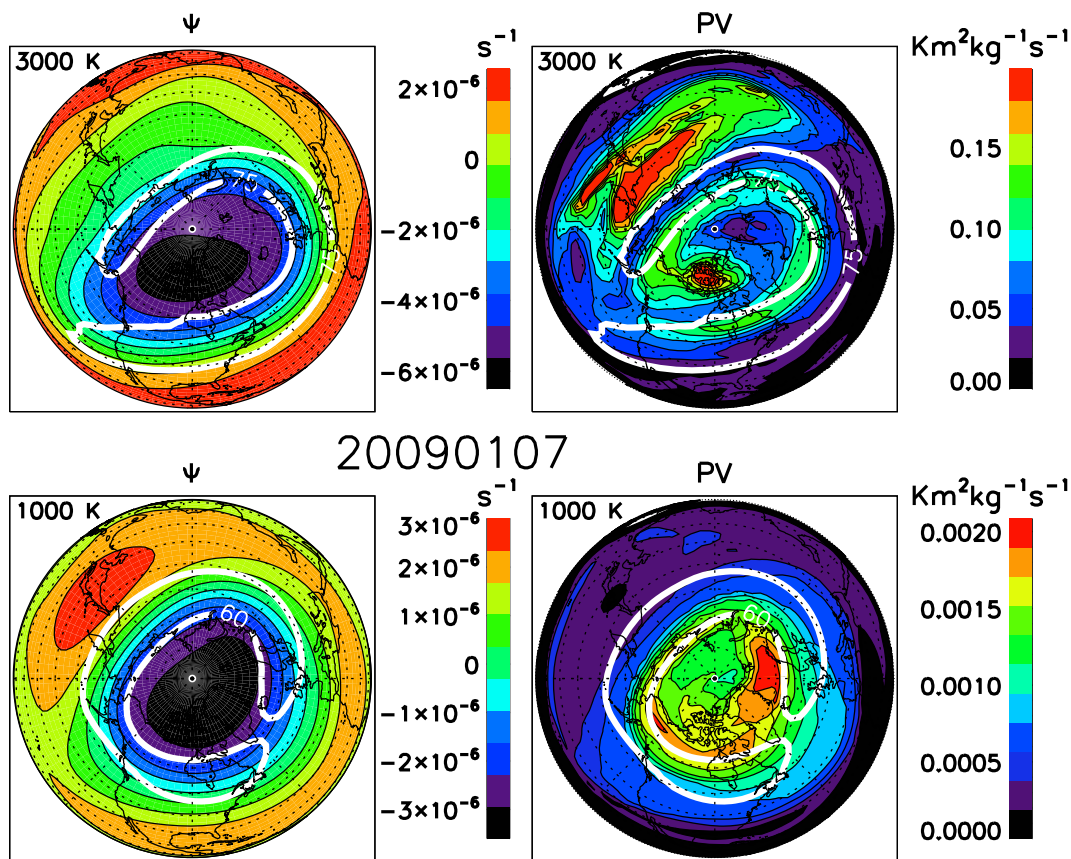


Figure 1. NH orthographic projections of GEOS-5 (left) ψ and (right) PV on 7 January 2009 at the (top) 3000 K level (~ 60 km) and (bottom) 1000 K level (~ 35 km). The thick white contour denotes wind speeds of 75 m/s at 3000 K and 60 m/s at 1000 K. The units for ψ are s^{-1} ; thus it needs to be multiplied by the radius of the Earth squared for use in calculating wind or vorticity.

of ψ and PV at two vertical levels on a typical boreal winter day. While conditions on this day are representative, the strongest stratospheric warming on record began ~ 12 days later [Manney *et al.*, 2009a]. The 1000 K surface (Figure 1, bottom) lies in the middle stratosphere near 35 km, while 3000 K (Figure 1, top) is in the lower mesosphere near 60 km. The thick, white contour overlaying the ψ and PV fields denotes the vortex jet as defined by the GEOS-5 analyses. Horizontal wind speeds exceed 75 (60) m/s inside this contour at 3000 K (1000 K). At 1000 K, streamlines (Figure 1, left) are parallel to the geostrophic flow and are thus aligned with the PNJ. ψ values decrease monotonically normal to the jet axis. Large PV gradients (Figure 1, right) are collocated with the PNJ and PV values increase poleward across the jet. However, there is a local PV minimum over the most of the Arctic Ocean. As a result, equivalent latitudes based on the PV field combine air in the vortex core with air near the jet stream (regions shaded green in Figure 1) and are placed into the same equivalent latitude bin. In this situation, 90° equivalent latitude does not correspond to air in the vortex core; instead, it denotes air along the poleward flank of the jet. An example of this effect on the interpretation of trace gas distributions is given by Feist *et al.* [2007] who showed dry mesospheric air in the Arctic vortex that had midlatitude (instead of high latitude) equivalent latitude values.

[16] At 3000 K, the PNJ remains pole-centered but is elongated along the 210° E and 30° E meridians. By definition, streamlines remain aligned with the horizontal flow and ψ values decrease monotonically poleward of the PNJ (Figure 1, top left). Figure 1 (top right) shows that the PV field is complicated. Maximum PV values stretch along the PNJ as well as over Asia and the North Pacific (equatorward of the jet stream). Large regions of low PV are located poleward of the jet maxima over the Arctic Ocean, north of Greenland. PV does not increase monotonically poleward of the jet due to decreased static stability above a distorted polar warm anomaly (shown in section 4). The explanation has at its core a fundamental dynamical setting of a warm pole in a westerly vortex, plus synoptic advection isolating PV pockets such that there are subregions where PV correlates positively with ψ . Caution must be used in the interpretation of small-scale structure since the temperature and wind fields suffer from inaccuracies due to a lack of observations constraining the model above the stratopause. High altitude PV fields in the National Center for Atmospheric Research Whole Atmosphere Community Climate Model also show high values that stretch along the poleward flank of the jet (not shown); this provides confidence that large-scale structures are realistic. Additionally, MLS PV fields show similar zonal bands of high values in midlatitudes [e.g., Manney *et al.*, 2008a,

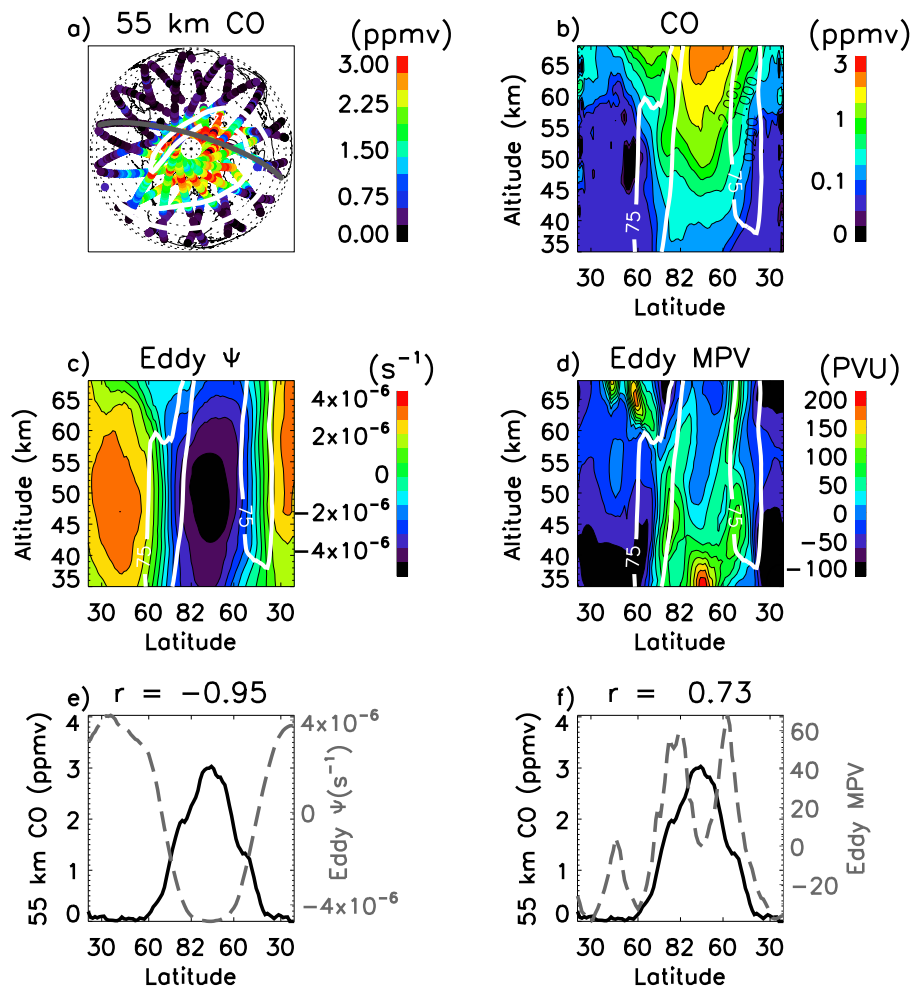


Figure 2. GEOS-5 ψ , PV, and MLS carbon monoxide on 7 January 2009. (a) NH polar stereographic projection of CO at 55 km, (b) cross-polar altitude section of CO along the MLS swath indicated with gray symbols in Figure 2a, (c) cross-polar altitude section of ψ minus the hemispheric mean at each altitude, (d) same as Figure 2c but for MPV, (e) CO (solid black curve) and ψ (dashed gray curve) along the cross-polar track at 55 km, and (f) CO (solid black curve) and MPV (dashed gray curve) along the track at 55 km. As in Figure 1, the white contours in Figures 2a–2d denote wind speeds of 75 km.

Figure 9] lending confidence that the large-scale structure of GEOS-5 PV is of sufficient quality for the purposes of this work.

[17] While there remain large PV gradients at the jet, allowing PV to adequately define the vortex edge on this day, the vortex itself contains a wide range of PV values. Similar to the 1000 K level (but to a larger degree), equivalent latitudes based on PV blend air in different dynamical regimes and thus diminish its primary advantage. Since there are both high and low PV values in the lowest ψ bins, the spatial correlation between ψ and PV breaks down. This work makes use of the correlation between ψ and PV to quantify how often maximum PV is not located in the lowest ψ bins. When this is the case, 90° equivalent latitude does not correspond to air in the vortex core.

[18] MLS CO is shown next as an independent data set with which to compare to GEOS-5 ψ and PV and explore variations with respect to the vortex. This analysis gives confidence that ψ is a reliable vortex-centered metric above 50 km where observations do not constrain the GEOS-5

analyses. Figure 1 showed ψ and PV at two altitudes: 35 km and 60 km. Figure 2 pertains to the same day as shown in Figure 1. Figure 2a is a NH polar stereographic projection of CO at 55 km. As in Figure 1, the white contour denotes the 75 m/s isotach surrounding the PNJ. Highest CO mixing ratios are located inside the vortex near the pole and rapidly decrease outside the vortex. The dark gray symbols in Figure 2a indicate the MLS swath that is the x axis in Figures 2a–2f. Figures 2b, 2c, and 2d are cross-polar altitude sections of MLS CO, GEOS-5 ψ , and GEOS-5 Modified PV (MPV), respectively. MPV is used here to reduce the exponential increase of PV with altitude to view horizontal variations in PV at multiple altitudes simultaneously [Lait, 1994]. GEOS-5 ψ and MPV have been interpolated to the MLS measurement locations. For clarity, the mean ψ and MPV poleward of 20° N at each altitude has been subtracted. The white contour in Figures 2b, 2c, and 2d denotes the 75 m/s isotach; this highlights the location of the PNJ between 35 km and 70 km. Figure 2b shows CO contours that are displaced downward at high latitudes and

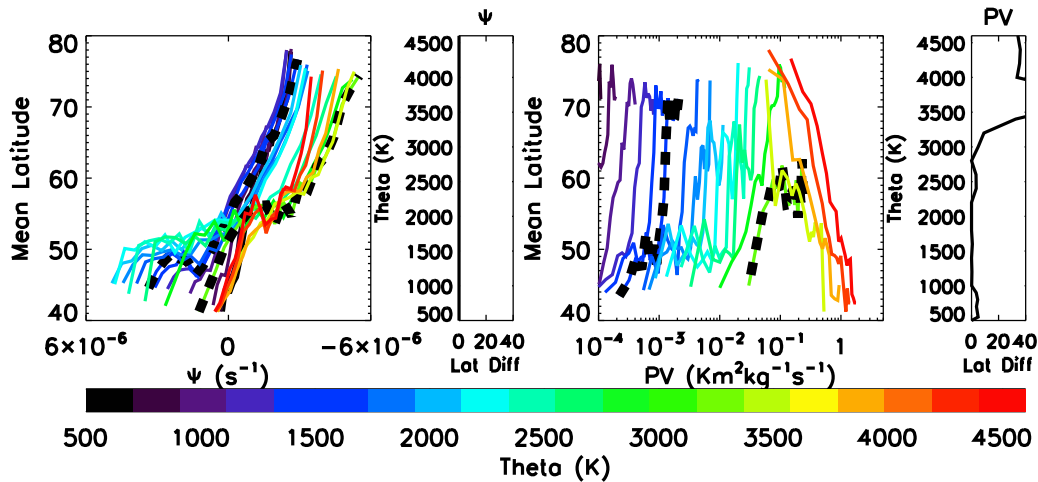


Figure 3. Mean latitude as a function of (left) ψ and (right) PV on 7 January 2009. Mean latitude is computed within 20 equally spaced ψ and PV bins based on the range of values observed poleward of 40°N latitude. Colors denote potential temperature levels between 500 K and 4500 K. Black dashed curves indicate the 1000 K and 3000 K levels shown in Figure 1. To the right of each plot is a vertical profile of the latitude difference between the mean latitude in the lowest ψ (highest PV) bin and the poleward-most mean latitude in any ψ (PV) bin.

indicate the descent of mesospheric air into the polar vortex. At each altitude, the highest CO values are collocated with the lowest ψ values at the corresponding altitude in Figure 2c. The alignment of CO and ψ contours suggests that the large-scale ψ field is realistic. Figure 2d shows that MPV is higher in the vortex below ~ 40 km, above which MPV maxima are located along the poleward flank of the jet. The vertical continuity of the two lobes of maximum PV suggests that the complex horizontal distribution shown in Figure 1 is physically consistent and not dominated by artifacts in the analyses. The local PV minima inside the vortex at altitudes as low as 40 km indicate that it is also not due to a lack of observations constraining the model. The ψ and MPV patterns shown here occur regularly throughout the winter in both hemispheres. Figures 2e and 2f show more quantitatively the relationship between CO, ψ , and MPV along the MLS swath at 55 km. Figure 2e is CO (solid black) and ψ (gray dashed). Figure 2f is CO as in Figure 2e and MPV (gray dashed). Figure 2e shows a strong anticorrelation (-0.95) between CO and ψ . Figure 2f shows that, to first order, MPV increases as CO increases and this results in a positive correlation of 0.73. However, local MPV maxima are collocated with the PNJ, equatorward of the CO maximum. Thus, highest equivalent latitudes correspond to air near the PNJ and lower values of equivalent latitude are in the vortex core. These results are consistent with *Lahoz et al.* [2009, Figure 6], who showed anticorrelations between PV and methane at 1900 K (~ 50 km) in the Antarctic vortex in April and May 2003.

[19] A key point in Figures 2c and 2d is that the vertical structure of ψ is deep (being a vertical integral of temperature), while the vertical structure of PV is more shallow (being a vertical derivative of temperature). Mesospheric ψ values “remember” the deep, cold polar stratosphere well into the lower mesosphere, while mesospheric PV values are influenced more by shallow temperature anomalies in the lower mesosphere.

[20] When the vortex encircles the pole, the mean geographic latitude within ψ and PV bins generally varies monotonically and this can be used as a first-order measure of how far PV maxima are from the pole. When filaments of high PV stretch along the subtropical jet, the maximum mean geographic latitude is not located in the highest PV bins. To evaluate how the mean geographic latitude varies as a function of PV and ψ , the area-weighted mean latitude for each PV and ψ bin is calculated. Mean latitude is computed within twenty equally spaced ψ and PV bins based on the range of values observed poleward of 40° N latitude. The latitude constraint is applied separately in each hemisphere. Figure 3 shows the mean latitude within NH ψ (Figure 3, left) and PV (Figure 3, right) bins between 500 K and 4500 K (~ 20 – 75 km) on the same day as shown in Figure 1. Each colored curve represents a different potential temperature. Black dashed curves indicate the potential temperature levels shown in Figure 1. Figure 3 (left) shows that mean latitude increases monotonically as ψ decreases on this day. Figure 3 (right) shows that below ~ 3000 K (purple and blue curves), mean latitude increases with increasing PV, as expected. However, above this altitude (yellow and red curves), the mean latitude decreases with increasing PV. This is consistent with the PV field shown in Figure 1 (top right), where maximum PV values are primarily located in mid-latitudes rather than in the vortex center. Above ~ 3000 K, PV is generally not “vortex-centered” even when the vortex jet is fairly zonally symmetric (as in Figure 1). At all altitudes, ψ decreases monotonically into the vortex core where horizontal winds are weak. Thus, it is appropriate to use ψ (or a long-lived tracer) to compute equivalent latitude throughout the stratosphere and lower mesosphere. This premise holds true even in situations when the vortex center is shifted from the pole and when the shape of the vortex is elongated. When the vortex is split, the physical interpretation of equivalent latitude is ambiguous regardless of the diagnostic on which it is based.

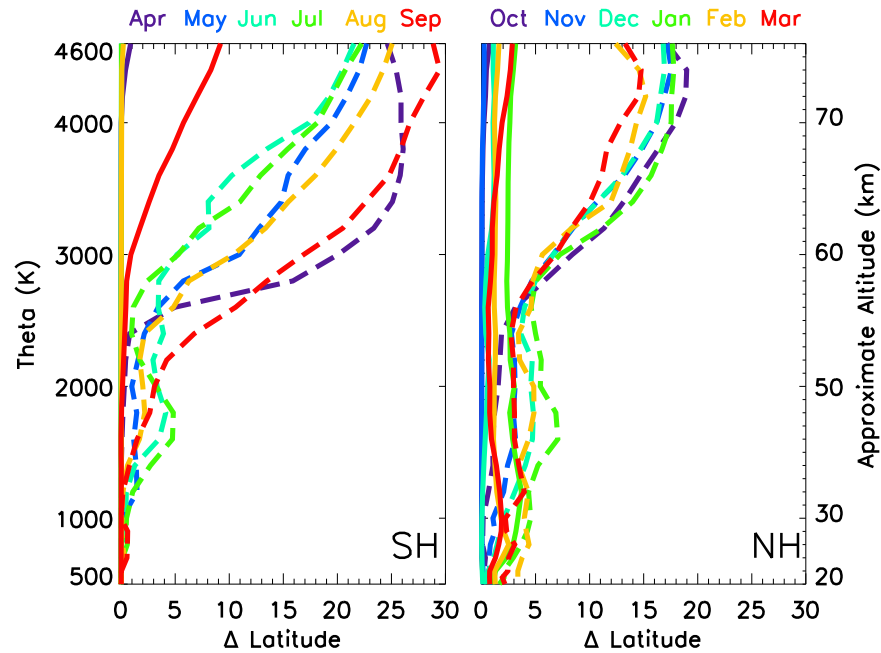


Figure 4. (left) SH and (right) NH multiyear (October 2003 to April 2009) monthly mean profiles of latitude differences based on ψ (solid curves) and PV (dashed curves). Latitude differences are shown as absolute values.

[21] For the example shown here we assume that ψ is vortex-centered at all altitudes. Thus, for PV to be vortex-centered the mean latitude in PV bins should correlate with the mean latitude in ψ bins and latitude differences between the two should be close to zero. At each altitude (i.e., for each of the colored curves) differences are computed between the mean latitude in the lowest ψ (highest PV) bin and the poleward-most mean latitude in any ψ (PV) bin. An altitude profile of these differences is shown to the right of each plot in Figure 3. Latitude differences based on ψ are zero at all altitudes. However, latitude differences based on PV increase to 10° at ~ 3000 K and to nearly 40° at 4000 K. Latitude differences larger than $\sim 10^\circ$ are associated with largest PV values that stretch along the subtropical jet and correspond to moderate values of ψ compared to the hemispheric average. At these altitudes, it is appropriate to use ψ to compute equivalent latitude.

[22] The negative relationship between ψ and latitude breaks down any time the vortex is not approximately pole centered. This is the case, e.g., during stratospheric warming events, during vortex formation and breakdown, and in the polar mesosphere. To estimate how often this occurs we compute average latitude differences in the 3000 K to 4500 K (~ 60 – 75 km) layer. In the NH, the layer average latitude differences exceed 10° by 2% in December, 6% in January, 4% in February, and 1% in March (not shown). In the Southern Hemisphere (SH), this occurs 14% of the time in September because the Antarctic vortex is displaced from the pole as the summer anticyclone descends into the stratosphere (but 0% of the time in the other months considered here). The results shown in Figure 4 are nearly identical when these days are included or excluded. Thus, the climatology that follows includes these events.

[23] In Figure 4, the daily latitude differences shown in Figure 3 are combined and presented as multiyear monthly

means. Solid (dashed) curves show ψ -based (PV-based) latitude difference profiles. Latitude differences are presented as absolute values. The months shown are restricted to when the vortex is generally well established. In the SH (Figure 4, left), latitude differences based on ψ are less than 1° at all altitudes during all winter months. Only in September, when the upper stratospheric vortex begins to break down, do the latitude differences increase. Latitude differences based on PV, on the other hand, increase from 3 to 5° below 2500 K to ~ 20 – 30° at 4000 K. Maximum latitude differences occur in April and September when the upper stratospheric vortex is displaced from the pole. The 5° maximum at ~ 1700 K in June and July is a regular recurring feature and is examined further in Section 4.

[24] In the NH (Figure 4, right), mean latitude differences based on ψ are $\leq 3^\circ$ at all altitudes. These differences are slightly larger than in the SH due to stratospheric warming events that occur at different times in different years. Latitude differences based on PV are $\sim 5^\circ$ below 2500 K and increase to $\sim 15^\circ$ at 4000 K. These results show the dramatic increase in the PV-based latitude differences above 3000 K in both hemispheres. At these altitudes, large positive (negative) PV values in the NH (SH) are often confined to zonal bands in midlatitudes, giving rise to large latitude differences.

[25] Figure 5 shows the relationship between PV and ψ at the same potential temperature levels and on the same day as shown in Figures 1, 2, and 3. Mean PV is computed within the same ψ bins as in Figure 3 and dashed curves indicate the potential temperature levels shown in Figure 1. The y axis is logarithmic, so small changes in the slope of the curves are significant. In the stratosphere (lower PV values), the predominant relationship between PV and ψ is an anticorrelation, but the correlation coefficient varies significantly with altitude and ψ value. A negative correla-

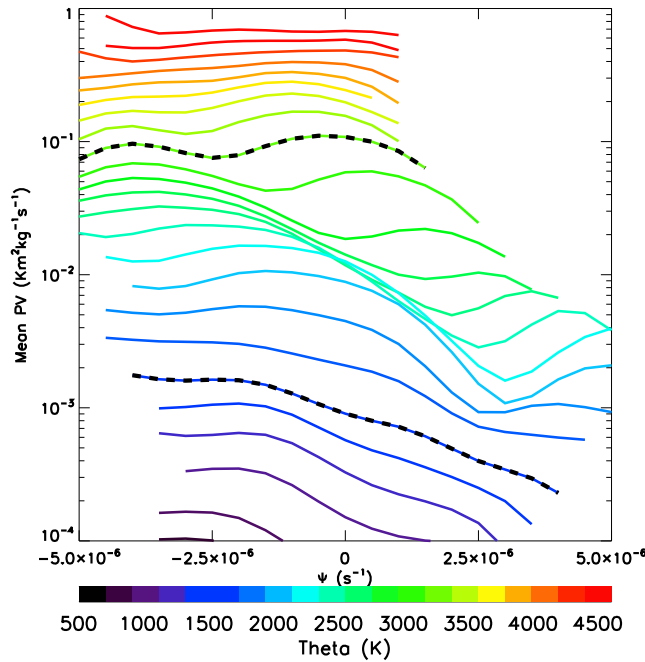


Figure 5. Mean PV as a function of ψ on 7 January 2009. Mean PV is computed within 20 equally spaced ψ bins based on the range of values observed poleward of 40°N latitude. Colors denote potential temperature levels between 500 K and 4500 K. Black dashed curves indicate the 1000 K and 3000 K levels shown in Figure 1.

tion dominates below 2000 K at all values of PV and ψ (PV increases as ψ decreases). However, a significant region of weak or positive correlation exists above ~ 2000 K in negative ψ bins (upper left corner of Figure 5). In the upper

stratosphere and lower mesosphere this relationship changes sign because maximum PV values are located in intermediate ψ bins instead of in the lowest (highest) ψ bins poleward of the jet. Here, we compute the fraction of the time (hereafter referred to as frequency) that the largest PV values are located in the upper half of ψ bins (lower half of ψ bins in the SH). The analysis is performed daily in each hemisphere as a function of potential temperature.

[26] In the NH (SH), we estimate how often PV maxima (minima) are observed in intermediate ψ bins in the subtropics and midlatitudes instead of in the lowest (highest) ψ bins poleward of the jet. Here, we compute the fraction of the time (hereafter referred to as frequency) that the largest PV values are located in the upper half of ψ bins (lower half of ψ bins in the SH). The analysis is performed daily in each hemisphere as a function of potential temperature.

[27] Figure 6 shows vertical profiles of multiyear monthly mean frequencies in the SH (Figure 6, left) and NH (Figure 6, right). Qualitatively, results in the two hemispheres are similar, showing generally increasing frequencies – and thus a greater incidence of “PV ribbons” in midlatitudes – with increasing altitude. Below ~ 2000 K (~ 50 km), largest PV values are located in subtropical or midlatitude ψ bins less than 10% (20%) of the time. At 3000 K (~ 60 km), largest PV values are observed in lower latitude ψ bins ~ 30 –50% of the time. At 4000 K (~ 70 km), this fraction reaches ~ 40 –80%.

4. Discussion

[28] This section explores how the correlation between PV and ψ can become zero or positive in the lower mesosphere. The utility of mapping constituents by PV is based on typical stratospheric observations showing PV and constituents covarying according to air mass type, which implicitly results from correlations in sources and sinks and

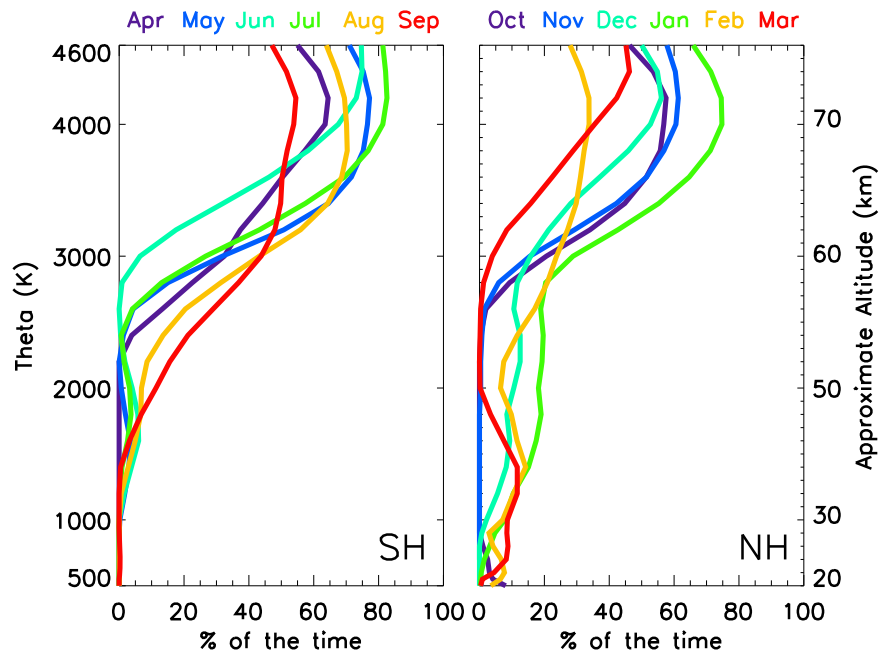


Figure 6. (left) SH and (right) NH multiyear (October 2003 to April 2009) monthly mean profiles of the fraction of the time that maximum (minimum) PV is located in the higher (lower) half of ψ bins, indicating how often PV is not vortex-centered.

mutual advection by winds. In the polar mesosphere, nonconservative processes [e.g., *Haynes and McIntyre, 1987*] acting uniquely on PV will alter its relationship with constituents. In the polar winter mesosphere, a descending warm anomaly, forced by the global pattern of mesospheric gravity wave drag, leads to an upward decrease in the strength of the PNJ and an equatorward displacement of the jet axis. Diabatic processes include strong radiative cooling and irreversible mixing by breaking gravity and Rossby waves. The nonlinear interaction between wave drag and the weak winds leads to descent of the warm anomaly [*Hitchman et al., 1989*]. The effect of this warm anomaly on the zonal wind, vorticity, static stability, and PV fields is described, and its effect on the correlation between PV and ψ is proposed.

[29] One may diagnose the effect of the polar warm anomaly on the distribution of PV (and ψ) through the thermal wind relation:

$$\partial u / \partial z = -g / (\theta f) \partial \theta / \partial y. \quad (2)$$

The poleward temperature increase leads to easterly shear with height ($\partial u / \partial z < 0$). Going upward into the mesospheric polar vortex, the vertical derivative of absolute vorticity, η , is

$$\partial \eta / \partial z = g / (\theta f) \partial^2 \theta / \partial y^2. \quad (3)$$

In the polar warm anomaly $\partial^2 \theta / \partial y^2 < 0$, so $f \partial \eta / \partial z < 0$, which implies smaller magnitude of absolute vorticity, tending to cause an upward decrease in PV into the mesosphere poleward of the jet maximum. Relative vorticity and ψ are related through the horizontal Laplacian. With suitable boundary conditions the two variables satisfy the invertibility principle and contain the same information. Hence vorticity alone would not alter the relationship between PV and ψ . One must therefore look to static stability for understanding how the correlation between PV and ψ can become zero or positive.

[30] One fundamental difference between PV and ψ is that ψ is a vertical integral of temperature, while PV includes a vertical derivative of temperature. This makes PV more responsive to local temperature structures than ψ . The poleward temperature decrease into the stratospheric winter polar vortex exists through a deep layer, and this relationship is preserved into the mesosphere in ψ . In contrast, the lower mesospheric warm anomaly implies decreased static stability above, which changes PV more than ψ , thereby altering $\partial P / \partial \psi$.

[31] Figure 7 illustrates the relationship between the warm anomaly and static stability and provides a comparison between GEOS-5 and MLS on 7 January 2009. Figures 7a, 7c, and 7e (Figures 7b, 7d, and 7f) is GEOS-5 (MLS). Figures 7a and 7b are NH polar projections of temperature at 65 km. The large-scale horizontal temperature structure is in good agreement; both GEOS-5 and MLS show a warm stratopause poleward of the jet (white contour) and low temperatures in the lower mesosphere equatorward of the jet. Also shown are cross-polar altitude sections of temperature (Figures 7c and 7d) and static stability (Figures 7e and 7f).

GEOS-5 temperature and static stability have been interpolated to the MLS measurement locations along the same swath shown in Figures 2b, 2c, and 2d. The temperature swaths show that the large-scale structure is in fairly good agreement between GEOS-5 and MLS, despite the complicated structure of the stratopause on this day. This level of agreement is often observed, except after the stratospheric warming/mesospheric cooling events in 2006 and 2009 [*Manney et al., 2008a, 2009a*]. Figures 7e and 7f show the large-scale structure of static stability is in general agreement between GEOS-5 and MLS. Static stability is generally larger poleward of the jet at all altitudes below ~ 60 km. However, both GEOS-5 and MLS show that, between 50 km and 60 km, there is a local PV minimum in the vortex with maxima near the jet. Lower static stability in the core of the mesospheric vortex is consistent with decreased PV above the polar warm anomaly. This feature is consistent with low PV in the vortex core relative to the jet (compare Figure 7e to Figure 2d).

[32] Figure 7 clearly illustrates that temperature anomalies in the lower mesospheric wave breaking regime are vertically local, leading to vertically local variations in PV. Meanwhile, ψ “remembers” the cold lower stratosphere well into the mesospheric polar vortex, leading to a change in the relationship between PV and ψ and a degradation of the utility of PV as a vortex-centered coordinate.

5. Conclusions

[33] GEOS-5 analyses are used to quantify how often PV varies monotonically across the jet and into the vortex. In the lower and middle stratosphere, both ψ and (usually) PV vary monotonically normal to the polar westerly jet (except when the vortex is extremely disturbed). Thus, it is often appropriate to interpret these fields as vortex-centered coordinate systems. The example shown in this work emphasizes that, at times, small PV values are located in the vortex core down to 40 km. This is largely a result of temperature generated static stability anomalies. Above ~ 3000 K (~ 60 km), ψ values continue to vary monotonically normal to the jet and to tracer contours. Thus, in the lower mesosphere the ψ field remains vortex-centered. Above ~ 3000 K (~ 60 km), PV does not vary monotonically with ψ up to 80% of the time. At these high altitudes, regions of small PV are often found in the vortex core and the largest positive (negative) values are found near the subtropical jet maximum in the NH (SH). This work supports the use of equivalent latitude based on ψ as a vortex-centered coordinate in the polar winter mesosphere.

[34] The extent to which PV varies monotonically across the jet toward the vortex core is quantified by calculating average latitude difference profiles between the mean latitude in the highest PV band and the most polar mean latitude within any of the PV bands in the hemisphere on each altitude and day. These differences are compared to ψ -based calculations performed in a similar manner. Latitude differences based on ψ are less than 3° up to 4600 K in both hemispheres (except in the SH in September when the vortex begins to breakdown in the upper stratosphere). In contrast, results based on PV show latitude differences on the order of 15° to 30° above 3000 K. While inaccuracies in the assimilated analyses at high altitudes may somehow

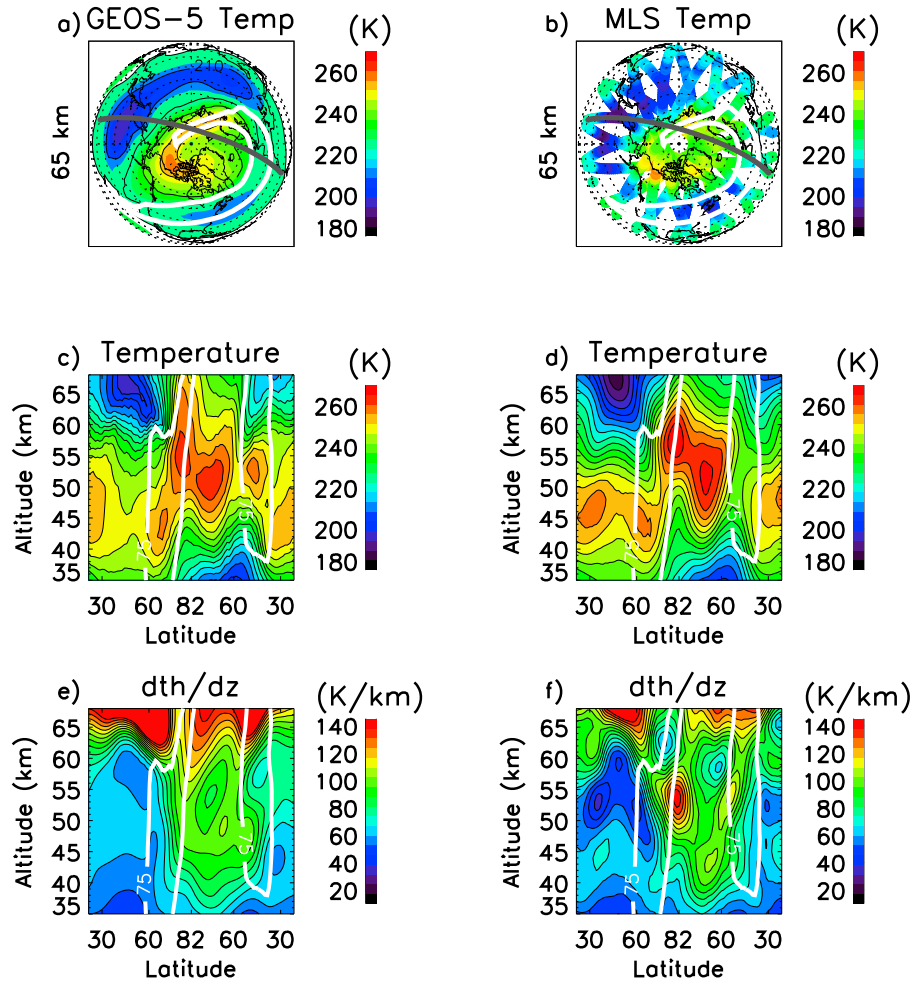


Figure 7. (left) GEOS-5 and (right) MLS temperature and static stability on 7 January 2009. (a and b) NH polar stereographic projections of temperature at 65 km, (c and d) cross-polar altitude sections of temperature along the MLS swath indicated with gray symbols in Figures 7a and 7b, and (e and f) the same as Figures 7c and 7d but for static stability. White contours in all plots denote wind speeds of 75 km.

foster decorrelation of PV and ψ , it is argued that the gravity wave driven warm anomaly causes PV magnitude to decrease poleward. It is further argued that radiative transfer and local heating rates can change the relationship between PV and ψ . The key theoretical point is that the changing relationship between ψ and PV depends critically on static stability changes. The lower mesospheric warm anomaly implies decreased static stability, which decreases PV more than ψ , thereby altering $\partial P/\partial \psi$. It is concluded that when there is a weak or positive correlation between PV and ψ (at any altitude) care should be taken when using PV as a vortex-centered coordinate, when defining the vortex edge using individual PV contours, and when using PV values to separate air masses that are inside from those that are outside the vortex. Future work will explore the implications of this result on other commonly used definitions of the vortex edge.

[35] **Acknowledgments.** We thank the Global Modeling and Assimilation Office at NASA's Goddard Space Flight Center for producing and distributing the analyses and the MLS Science Team for providing the MLS

data. We would also like to thank Duncan Fairlie, who provided the code to compute ψ , and Steven Pawson for useful discussions about the GEOS-5 analyses. We appreciate comments from three anonymous reviewers that significantly improved the quality of this manuscript. V.L.H. was supported by NASA's New Investigator Program grant NNN05ZDA001N, C.E.R. was supported by NASA LWS grant NNX06AC05G, and M.H.H. was supported by NASA grant NNX08AW52G.

References

- Allen, D. R., and N. Nakamura (2003), Tracer equivalent latitude: A diagnostic tool for isentropic transport studies, *J. Atmos. Sci.*, **60**(2), 287–304, doi:10.1175/1520-0469(2003)060<0287:TELADT>2.0.CO;2.
- Andrews, D. G., J. R. Holton, and C. B. Leovy (1987), *Middle Atmosphere Dynamics*, 489 pp., Academic Press, San Diego, Calif.
- Baldwin, M. P., and J. Holton (1988), Climatology of the stratospheric polar vortex and planetary wave breaking, *J. Atmos. Sci.*, **45**, 1123–1142, doi:10.1175/1520-0469(1988)045<1123:COTSPV>2.0.CO;2.
- Bloom, S., L. Takacs, A. DaSilva, and D. Ledvina (1996), Data assimilation using incremental analysis updates, *Mon. Weather Rev.*, **124**, 1256–1271, doi:10.1175/1520-0493(1996)124<1256:DAUIAU>2.0.CO;2.
- Butchart, N., and E. Remsberg (1986), The area of the stratospheric polar vortex as a diagnostic for tracer transport on an isentropic surface, *J. Atmos. Sci.*, **43**, 1319–1339, doi:10.1175/1520-0469(1986)043<1319:TAOTSP>2.0.CO;2.
- Danielsen, E. F. (1990), In defense of Ertel potential vorticity and its general applicability as a meteorological tracer, *J. Atmos. Sci.*, **47**(16), 2013–2020, doi:10.1175/1520-0469(1990)047<2013:IDOEPV>2.0.CO;2.

- Dunkerton, T. J., and D. P. Delisi (1985), The subtropical mesospheric jet observed by the Nimbus 7 Limb Infrared Monitor of the Stratosphere, *J. Geophys. Res.*, **90**, 10,681–10,692, doi:10.1029/JD090iD06p10681.
- Ertel, H. (1942), Ein neuer hydrodynamischer wirbelsatz, *Meteorol. Z.*, **59**, 277–281.
- Feist, D. G., A. J. Geer, S. Muller, and N. Kampfer (2007), Middle atmosphere water vapour and dynamical features in aircraft measurements and ECMWF analyses, *Atmos. Chem. Phys.*, **7**, 5291–5307.
- Filipiak, M., et al. (2005), Carbon monoxide measured by the EOS Microwave Limb Sounder on Aura: First results, *Geophys. Res. Lett.*, **32**, L14825, doi:10.1029/2005GL022765.
- Fisher, M., et al. (1993), Rapid descent of mesospheric air into the stratospheric polar vortex, *Geophys. Res. Lett.*, **20**, 1267–1270, doi:10.1029/93GL01104.
- Garcia, R. R., and B. A. Boville (1994), “Downward control” of the mean meridional circulation and temperature distribution of the polar winter stratosphere, *J. Atmos. Sci.*, **51**, 2238–2245, doi:10.1175/1520-0469(1994)051<2238:COTMMC>2.0.CO;2.
- Harvey, V. L., R. B. Pierce, and M. H. Hitchman (2002), A climatology of stratospheric polar vortices and anticyclones, *J. Geophys. Res.*, **107**(D20), 4442, doi:10.1029/2001JD001471.
- Haurwitz, B. (1961), Frictional effects and the meridional circulation in the mesosphere, *J. Geophys. Res.*, **66**, 2381–2391, doi:10.1029/JZ066i008p02381.
- Haynes, P., and M. McIntyre (1987), On the evolution of vorticity and potential vorticity in the presence of diabatic heating and frictional or other forces, *J. Atmos. Sci.*, **44**, 828–841, doi:10.1175/1520-0469(1987)044<0828:OTEOVA>2.0.CO;2.
- Hitchman, M. H., and A. S. Huesmann (2007), A seasonal climatology of Rossby wave breaking in the 320–2000-K layer, *J. Atmos. Sci.*, **64**, 1922–1940, doi:10.1175/JAS3927.1.
- Hitchman, M. H., J. C. Gille, C. D. Rodgers, and G. Brasseur (1989), The separated polar winter stratopause: A gravity wave driven climatological feature, *J. Atmos. Sci.*, **46**, 410–422, doi:10.1175/1520-0469(1989)046<0410:TSPWSA>2.0.CO;2.
- Hoskins, B. J., M. E. McIntyre, and A. W. Robertson (1985), On the use and significance of isentropic potential vorticity maps, *Q. J. R. Meteorol. Soc.*, **111**, 877–946, doi:10.1256/smsqj.47001.
- Lahoz, W. A., et al. (1994), Three-dimensional evolution of water-vapor distributions in the northern-hemisphere stratosphere as observed by the MLS, *J. Atmos. Sci.*, **51**, 2914–2930, doi:10.1175/1520-0469(1994)051<2914:TDEOWV>2.0.CO;2.
- Lahoz, W. A., et al. (2009), Mesosphere-stratosphere transport during Southern Hemisphere autumn deduced from MIPAS observations, *Q. J. R. Meteorol. Soc.*, **135**, 681–694, doi:10.1002/qj.397.
- Lait, L. R. (1994), An alternative form for potential vorticity, *J. Atmos. Sci.*, **51**, 1754–1759, doi:10.1175/1520-0469(1994)051<1754:AAFFPV>2.0.CO;2.
- Lary, D. J., et al. (1995), Three dimensional tracer initialization and general diagnostics using equivalent PV latitude-potential temperature coordinates, *Q. J. R. Meteorol. Soc.*, **121**, 187–210.
- Leovy, C. B. (1964), Simple models of thermally driven mesospheric circulation, *J. Atmos. Sci.*, **21**, 327–341, doi:10.1175/1520-0469(1964)021<0327:SMOTDM>2.0.CO;2.
- Lin, S.-J. (2004), A vertically Lagrangian finite-volume dynamical core for global models, *Mon. Weather Rev.*, **132**, 2293–2307, doi:10.1175/1520-0493(2004)132<2293:AVLFDC>2.0.CO;2.
- Livesey, N. J., et al. (2007), EOS MLS version 2.2 level 2 data quality and description document, *Tech. Rep. D-33509*, 115 pp., Jet Propul. Lab., Calif. Inst. of Technol., Pasadena, Calif.
- Manney, G. L., R. Zurek, A. O'Neill, and R. Swinbank (1994), On the motion of air through the stratospheric polar vortex, *J. Atmos. Sci.*, **51**, 2973–2994, doi:10.1175/1520-0469(1994)051<2973:OTMOAT>2.0.CO;2.
- Manney, G. L., H. A. Michelsen, M. L. Santee, M. R. Gunson, F. W. Irion, A. E. Roche, and N. J. Livesey (1999), Polar vortex dynamics during spring and fall diagnosed using trace gas observations from the Atmospheric Trace Molecule Spectroscopy instrument, *J. Geophys. Res.*, **104**, 18,841–18,866, doi:10.1029/1999JD900317.
- Manney, G. L., et al. (2007), Solar occultation satellite data and derived meteorological products: Sampling issues and comparisons with Aura Microwave Limb Sounder, *J. Geophys. Res.*, **112**, D24S50, doi:10.1029/2007JD008709.
- Manney, G. L., et al. (2008a), The evolution of the stratopause during the 2006 major warming: Satellite data and assimilated meteorological analyses, *J. Geophys. Res.*, **113**, D11115, doi:10.1029/2007JD009097.
- Manney, G. L., et al. (2008b), The high Arctic in extreme winters: Vortex, temperature, and MLS and ACE-FTS trace gas evolution, *Atmos. Chem. Phys.*, **8**, 505–522.
- Manney, G. L., M. J. Schwartz, K. Krüger, M. L. Santee, S. Pawson, J. N. Lee, W. H. Daffer, R. A. Fuller, and N. J. Livesey (2009a), Aura Microwave Limb Sounder observations of dynamics and transport during the record-breaking 2009 Arctic stratospheric major warming, *Geophys. Res. Lett.*, **36**, L12815, doi:10.1029/2009GL038586.
- Manney, G. L., et al. (2009b), Satellite observations and modeling of transport in the upper troposphere through the lower mesosphere during the 2006 major stratospheric sudden warming, *Atmos. Chem. Phys.*, **9**, 4775–4795.
- McFarlane, N. A. (1987), The effect of orographically excited gravity wave drag on the general circulation of the lower stratosphere and troposphere, *J. Atmos. Sci.*, **44**, 1775–1800, doi:10.1175/1520-0469(1987)044<1775:TEOOEG>2.0.CO;2.
- McIntyre, M. E., and T. N. Palmer (1983), Breaking planetary waves in the stratosphere, *Nature*, **305**, 593–600, doi:10.1038/305593a0.
- Nakamura, N. (1995), Modified Lagrangian-mean diagnostics of the stratospheric polar vortices. 1. Formulation and analysis of GFDL SKYHI GCM, *J. Atmos. Sci.*, **52**, 2096–2108, doi:10.1175/1520-0469(1995)052<2096:MLMDOT>2.0.CO;2.
- Nakamura, N., and J. Ma (1997), Modified Lagrangian-mean diagnostics of the stratospheric polar vortices. 2. Nitrous oxide and seasonal barrier migration in the cryogenic limb array etalon spectrometer and SKYHI general circulation model, *J. Geophys. Res.*, **102**, 25,721–25,735, doi:10.1029/97JD02153.
- Nash, E. R., P. A. Newman, J. E. Rosenfield, and M. R. Schoeberl (1996), An objective determination of the polar vortex using Ertel's potential vorticity, *J. Geophys. Res.*, **101**, 9471–9478, doi:10.1029/96JD00066.
- Norton, W. A. (1994), Breaking Rossby waves in a model stratosphere by a vortex-following coordinate system and a technique for advecting material contours, *J. Atmos. Sci.*, **51**, 654–673, doi:10.1175/1520-0469(1994)051<0654:BRWIAM>2.0.CO;2.
- Oberheide, J., H.-L. Liu, O. A. Gusev, and D. Offermann (2006), Mesospheric surf zone and temperature inversion layers in early November 1994, *J. Atmos. Terr. Phys.*, **68**, 1752–1763, doi:10.1016/j.jastp.2005.11.013.
- Proffitt, M. H., S. Solomon, and M. Loewenstein (1992), Comparison of 2-D model simulations of ozone and nitrous oxide at high latitudes with stratospheric measurements, *J. Geophys. Res.*, **97**, 939–944.
- Pumphrey, H. C., et al. (2007), Validation of middle-atmosphere carbon monoxide retrievals from the Microwave Limb Sounder on Aura, *J. Geophys. Res.*, **112**, D24S38, doi:10.1029/2007JD008723.
- Randall, C. E., et al. (2005), Reconstruction and simulation of stratospheric ozone distributions during the 2002 austral winter, *J. Atmos. Sci.*, **62**, 748–764, doi:10.1175/JAS-3336.1.
- Randall, C. E., V. L. Harvey, C. S. Singleton, P. F. Bernath, C. D. Boone, and J. U. Kozyra (2006), Enhanced NO_x in 2006 linked to strong upper stratospheric Arctic vortex, *Geophys. Res. Lett.*, **33**, L18811, doi:10.1029/2006GL027160.
- Randall, C. E., V. L. Harvey, C. S. Singleton, S. M. Bailey, P. F. Bernath, M. Codrescu, H. Nakajima, and J. M. Russell III (2007), Energetic particle precipitation effects on the Southern Hemisphere stratosphere in 1992–2005, *J. Geophys. Res.*, **112**, D08308, doi:10.1029/2006JD007696.
- Randall, C. E., V. L. Harvey, D. E. Siskind, J. France, P. F. Bernath, C. D. Boone, and K. A. Walker (2009), NO_x descent in the Arctic middle atmosphere in early 2009, *Geophys. Res. Lett.*, **36**, L18811, doi:10.1029/2009GL039706.
- Ren, R. C., and M. Cai (2006), Polar vortex oscillation viewed in an isentropic potential vorticity coordinate, *Adv. Atmos. Sci.*, **23**(6), 884–900, doi:10.1007/s00376-006-0884-6.
- Rhines, P. B., and W. R. Young (1982), Homogenization of potential vorticity in planetary gyres, *J. Fluid Mech.*, **122**, 347–367, doi:10.1017/S0022112082002250.
- Rienecker, M. M., et al. (2008), The GEOS-5 Data Assimilation System—Documentation of versions 5.0.1 and 5.1.0, *NASA Tech. Memo., NASA/TM-2007-104606*, vol. 27, 92 pp.
- Rosenfield, J. E., P. A. Newman, and M. R. Schoeberl (1994), Computations of diabatic descent in the stratospheric polar vortex, *J. Geophys. Res.*, **99**, 16,677–16,689, doi:10.1029/94JD01156.
- Rummukainen, M., B. Knudsen, and P. Vonderghaten (1994), Dynamical diagnostics of the edges of the polar vortices, *Ann. Geophys.*, **12**, 1114–1118.
- Sassi, F., R. R. Garcia, B. A. Boville, and H. Liu (2002), On temperature inversions and the mesospheric surf zone, *J. Geophys. Res.*, **107**(D19), 4380, doi:10.1029/2001JD001525.
- Schoeberl, M. R., et al. (1992), The structure of the polar vortex, *J. Geophys. Res.*, **97**, 7859–7882.
- Schwartz, M. J., et al. (2008), Validation of the Aura Microwave Limb Sounder temperature and geopotential height measurements, *J. Geophys. Res.*, **113**, D15S11, doi:10.1029/2007JD008783.
- Solomon, S. (1999), Stratospheric ozone depletion: A review of concepts and history, *Rev. Geophys.*, **37**, 275–316, doi:10.1029/1999RG000008.

- Stajner, I., N. Winslow, R. B. Rood, and S. Pawson (2004), Monitoring of observation errors in the assimilation of satellite ozone data, *J. Geophys. Res.*, *109*, D06309, doi:10.1029/2003JD004118.
- Stajner, I., C. Benson, H.-C. Liu, S. Pawson, N. Brubaker, L.-P. Chang, L. P. Riishojgaard, and R. Todling (2007), Ice polar stratospheric clouds detected from assimilation of Atmospheric Infrared Sounder data, *Geophys. Res. Lett.*, *34*, L16802, doi:10.1029/2007GL029415.
- Stan, C., and D. A. Randall (2007), Potential vorticity as meridional coordinate, *J. Atmos. Sci.*, *64*(2), 621–633, doi:10.1175/JAS3839.1.
- Waters, J. W., et al. (2006), The Earth Observing System Microwave Limb Sounder (EOS MLS) on the Aura satellite, *IEEE Trans. Geosci. Remote Sens.*, *44*, 1075–1092, doi:10.1109/TGRS.2006.873771.
- Waugh, D. W. (1997), Elliptical diagnostics of stratospheric polar vortices, *Q. J. R. Meteorol. Soc.*, *123*, 1725–1748, doi:10.1002/qj.49712354213.
- Wu, W.-S., R. J. Purser, and D. F. Parish (2002), Three-dimensional variational analyses with spatially inhomogeneous covariances, *Mon. Weather Rev.*, *130*, 2905–2916, doi:10.1175/1520-0493(2002)130<2905:TDVAWS>2.0.CO;2.
- V. L. Harvey and C. E. Randall, Laboratory for Atmospheric and Space Physics, University of Colorado at Boulder, UCB 392, Boulder, CO 80309-0392, USA. (lynn.harvey@lasp.colorado.edu)
- M. H. Hitchman, Department of Atmospheric and Oceanic Sciences, University of Wisconsin-Madison, Madison, WI 53706, USA.